

Cite this: *Phys. Chem. Chem. Phys.*, 2012, **14**, 10979–10986

www.rsc.org/pccp

PAPER

Ion transport in a class of imidazole-based liquid/solid protic ionics†

Vincenzo Tricoli,* Gabriele Orsini and Martina Anselmi

Received 30th March 2012, Accepted 31st May 2012

DOI: 10.1039/c2cp41027c

A class of protic ionic-compounds were prepared by Brønsted acid–base reaction of imidazole or benzimidazole with one of the following acids: trifluoromethanesulfonic, nonafluorobutanesulfonic, *para*-toluenesulfonic and trifluoroacetic. Except those based on trifluoroacetic acid, all prepared compounds are thermally stable up to at least 270 °C. They are solid up to temperatures between 134 and 220 °C, depending on their constituent acid and base. A simple physico-mathematical model of ion motion in the lattice was developed and implemented to correctly interpret frequency-dependent electrical response of these materials, particularly in the solid state, and investigate their ion-conducting behavior as a function of temperature. These ionic compounds display sensible ionic conductivity up to *ca.* 5×10^{-4} and 5×10^{-2} S cm⁻¹ in the solid and molten state, respectively, under fully anhydrous conditions. The presence of absorbed water, after brief exposure to an ambient atmosphere, enhances conduction properties remarkably. Conductivity values up to 10^{-3} and 10^{-1} S cm⁻¹ were registered, respectively, in the solid and molten state, after short exposure to (humid) ambient air. It is argued how absorbed water molecules may remove protons from (ImH)⁺ or (BImH)⁺ groups, thereby enabling a chain mechanism of proton-hopping through non-protonated Im or BIm sites. It is discussed how these results and methods may inspire designing protic ionic-materials at the solid-state, with enhanced proton conduction even under fully-anhydrous conditions.

Introduction

There is continuing interest in fuel cells operating at low temperature (<100 °C) because they have the potential to produce electrical energy *in situ* even at small scale with good efficiency and low impact on the environment.^{1,2} They can utilize either hydrogen or certain electrochemically active hydrocarbons (typically methanol) as the fuel. In the latter case carbon monoxide (CO) is formed at an intermediate stage during electro-oxidation of the hydrocarbon at an anode. A trace-amount of CO is often present even in a hydrogen feed, as the latter is generally produced *in situ* by hydrocarbon reforming. CO is a formidable poison for the anode catalyst, drastically affecting fuel-cell performance in terms of output voltage, delivered power and energy efficiency.³ That has motivated a vast research effort aimed at developing an anode catalyst with adequate resistance towards CO. Such catalysts are typically based on Pt–Ru alloys.⁴ It was also observed that CO tolerance greatly increases when the operating temperature is risen from say 80 °C to 180 °C.⁵ So, development of medium-temperature fuel cells operating in the range of 140–200 °C is

attracting increasing attention.⁶ However, the proton-conducting membrane suffers intolerable conductivity drop at such elevated temperature, due to dehydration. That prompted the search for proton-conducting materials able to work under anhydrous conditions as well.^{7,8} In recent years ionic liquids (ILs) have been proposed as potentially suitable materials for operation at elevated temperature as the presence of water is not necessary for ion conduction to occur.^{9–11} Moreover, they are generally non-volatile and thermally stable. Protic ionic liquids (PILs) are formed by combination of Brønsted acids and bases. They are better suited than non-protic ILs for fuel-cell applications as the conduction process involves transport of protons. A variety of PILs were prepared from various aliphatic amines with acids and investigated with respect to properties relevant to fuel cell applications, namely thermal stability, hydrophobicity, ionic-conductivity and electroactivity for hydrogen electro-oxidation and oxygen electro-reduction.^{12,13} Some PILs displayed a maximum ionic conductivity for non-stoichiometric combination of the acid with the base.¹⁴ Particularly, an excess of base can determine remarkably higher conductivity as compared to the neutral salt. That was shown to be a consequence of fast proton transfer between the protonated and non-protonated base molecules.¹⁵ However, in general, the non-protonated excess base is also relatively volatile, which could make non-stoichiometric PILs unsuitable for fuel-cell application. Moreover, reverse acid–base reaction may occur at elevated temperature for

Department of Chemical Engineering and Materials Science,
Università di Pisa, largo L. Lazzarino, 1, I-56122, Pisa, Italy.
E-mail: v.tricoli@diiccim.unipi.it

† Electronic supplementary information (ESI) available. See DOI: 10.1039/c2cp41027c

PILs formed by an insufficiently strong base or acid. In such a case the PIL, though stoichiometric, is not fully ionized, thereby becoming somewhat volatile.

In this work we prepared a class of imidazole-based protic ionic compounds (PICs) by stoichiometric combination of either imidazole (Im) or benzimidazole (BIm) with one of the following acids: trifluoromethanesulfonic (TFS), nonafluorobutanesulfonic (NFS), *para*-toluenesulfonic (*p*-TS) and trifluoroacetic (TFA). The choice of Im and BIm as the base was motivated by their amphoteric nature, similar to water: a nitrogen atom in position 3 has moderate basic characteristics ($pK_b = 7$ for Im and 5.5 for BIm), whereas proton bound to nitrogen in position 1 is weakly acidic ($pK_a = 14$ for Im and 12.8 for BIm).^{16–18} The co-presence of a basic and acidic site could in principle enable ionic conduction by an efficient proton-hopping chain-mechanism involving rupture and formation of N–H bonds.¹⁹ Except for TFA, the above acids have been chosen because of their strong characteristics, which should guarantee full ionic dissociation, *i.e.* negligible PIC volatility, even at the elevated temperatures, required for efficient catalyst operation in fuel-cells. Thermal stability was assessed by thermo-gravimetric analysis, whereas solid–liquid transitions were investigated by differential scanning calorimetry. Electrochemical impedance spectroscopy was utilized to elucidate ion transport mechanisms both in the solid and liquid state and investigate ionic conductivity.

Experimental

Materials and preparation methods

All bases (Im 99%, BIm 98%) and acids (TFA 99%, TFS 98%, NFS 97%, *p*-TS 98.5%) were used as received. PICs were prepared by straightforward acid–base reaction, in full analogy with previous works addressing preparation of novel ion-conducting PILs.^{13–15} First, a predetermined amount of the base was dissolved in a few ml of ethanol (99.9%). The solution was cooled down and maintained at 0 °C in an ice/water-bath. Then, an equimolar amount of acid was added (**caution:** acid addition must be made drop-wise as the reaction is strongly exothermic). As *p*-TS is a solid at room temperature, it was first dissolved in a water–ethanol mixture; then the solution was added slowly to the base solution. The resulting mixtures were kept under stirring for a few hours; then, most of the solvent was evaporated by slowly heating up to 100 °C in an oil-bath, thereby obtaining a white, sticky solid. Residual solvent was removed by drying overnight in a vacuum oven (10^{-2} torr) at 120 °C. All prepared products were hygroscopic; accordingly, they were stored in a silica-gel desiccator until characterization.

Physical characterization

Thermogravimetric analysis (TGA) on a TA instrument (mod. TGA Q500) thermobalance was performed for all prepared compounds to assess thermal stability. A predetermined sample amount of 10–15 mg was placed in an aluminum crucible and heated from room temperature to 350 °C at a heating rate of 20 °C min⁻¹ under air flow (sample gas 60 ml min⁻¹ and balance gas 40 ml min⁻¹).

Differential scanning calorimetry (DSC) on a Perkin-Elmer instrument (mod. Pyris 1) was utilized to determine melting

temperature and perhaps detect the possible presence of transitions at the solid state (*e.g.* crystalline–glassy transitions). The sample was heated up to 200 °C (or 250 °C depending on melting point) and maintained at the maximum temperature for 5 min. Then, it was cooled down to –5 °C and maintained at that temperature for 5 min. The scan-rate during heating or cooling was 20 °C min⁻¹. The thermal cycle was repeated once in order to be sure that no thermal degradation occurred during heating.

Crystallinity below melting point was assessed by powder X-ray diffraction (XRD) on a Siemens automatic diffractometer (mod. 810) using Cu–K α radiation and also by scanning electron microscopy (SEM) on a JEOL JSM 5600 operating at 15 kV.

Ionic conductivity

Ionic-conduction properties were investigated by electrical impedance spectroscopy (EIS). Cylindrical pellets (6 mm in diameter and 2.5 mm in thickness) for impedance measurements were formed by cold-pressing *ca.* 0.12 g of product at 300 MPa for 5 min in a hard-steel mould. The pellet was lodged into a circular ring of same inner diameter and height and then seal-locked between two mirror-finished, stainless-steel electrodes in a home-made cell made of glass-fiber-reinforced PEEK. The ring, also made of the same material, ensures that pellet shape and size remain unchanged even above melting point during high-temperature measurements. In order to ensure fully-anhydrous conditions, the pellet was first lodged in the unlocked impedance cell and kept at 120 °C under vacuum (10^{-2} torr) overnight. Then the cell was rapidly seal-locked in the oven itself. To assess influence of water humidity on ionic conductivity, pellets were also prepared from powders that had shortly been exposed (few minutes) to (humid) ambient air. Such pellets were not subjected to the above-mentioned anhydridification procedure before being sealed into the EIS test-cell. Impedance experiments were carried out at controlled temperature using a thermostating oil-bath. Impedance data were collected on a 1287 Solartron Electrochemical Interface connected to a 1255 Solartron Frequency Response Analyzer. An oscillating voltage of 10 mV was applied with amplitude and frequency ranging from 0.1 to 10⁶ Hz. Blank-cell impedance was obtained accounting for analyzer cables and was subtracted from all spectra prior to data elaboration. A physico-mathematical model, described further below, was developed to interpret electrochemical impedance spectra and determine ionic conductivity.

Results and discussion

All prepared PICs were solid at room temperature. They were also soluble both in water and ethanol, except (BImH)⁺(NFS)⁻, which was water-insoluble. Also, they were crystalline in the solid state as evidenced by XRD. As an example the XRD pattern of (ImH)⁺(*p*-TS)⁻ is displayed in Fig. 1. SEM was carried out on the fractured surface of bulk solids prepared by melting the powder and subsequent solidification. A layered morphology is exhibited, consistent with a crystalline structure (Fig. 2).

Thermal stability

Fig. 3 displays thermogravimetric curves for the four benzimidazole-based PICs. (BImH)⁺(TFS)⁻ and (BImH)⁺(NFS)⁻ are essentially stable up to at least 350 °C. They start losing

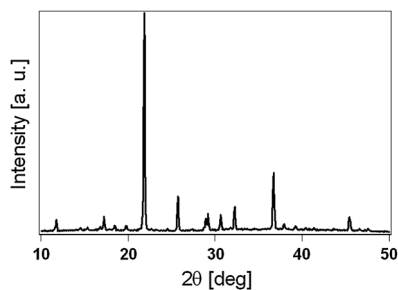


Fig. 1 XRD pattern of the $(\text{ImH})^+(\text{p-TS})^-$ sample.

weight above 270 °C. However, the total weight loss at 350 °C is inferior to 1.5%. A mass loss of the $(\text{BImH})^+(\text{p-TS})^-$ sample sets on at 200 °C and is about 1% at 270 °C. It becomes more consistent above 270 °C with a total weight loss of ca. 14% at 350 °C. Conversely, $(\text{BImH})^+(\text{TFA})^-$ is not thermally stable above 150 °C, with the mass completely vanished at about 250 °C. The thermogravimetric curves of the four imidazole-based ionics (shown in Fig. S1 in the ESI†) are correspondingly analogous to those in Fig. 3. Such a trend of thermal behavior is understood on the basis of strength of the Brønsted acid. In fact, the product is non-volatile when fully ionized. Complete ionization occurs at all temperatures for sufficiently strong Brønsted acid. For moderate acid-strength, chemical equilibrium may establish at sufficiently high temperature because of strong exothermicity of acid–base reaction, with re-constitution of the pristine, undissociated

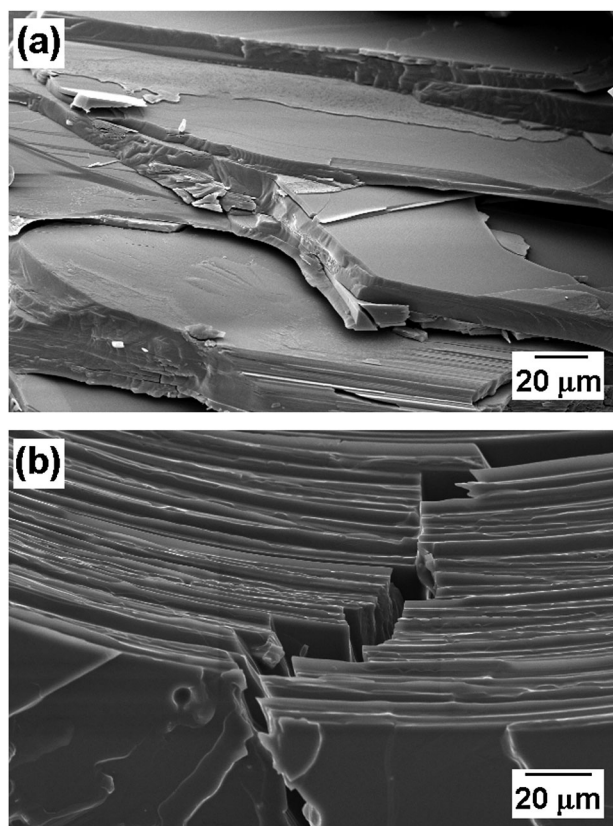


Fig. 2 SEM micrographs of samples (a) $(\text{BImH})^+(\text{NFS})^-$ and (b) $(\text{BImH})^+(\text{p-TS})^-$.

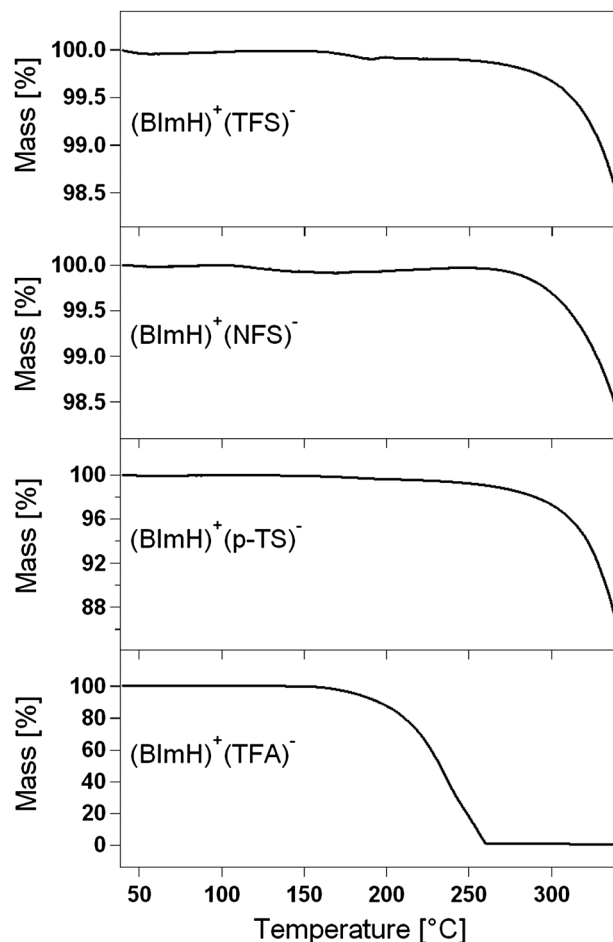


Fig. 3 Thermogravimetric curves for the benzimidazole-based PICs.

acid and base. As these are both volatile, the PICs become unstable at such elevated temperatures. Now, both TFS and NFS are strong acids with $\text{p}K_{\text{a}} \approx -15$, which accounts for the observed stability of the corresponding PICs up to at least 350 °C. *p-TS* exhibits moderately strong acidity ($\text{p}K_{\text{a}} \approx -2.8$) and that is consistent with the somewhat lower decomposition temperature of $(\text{BImH}$ or $\text{ImH})^+(\text{p-TS})^-$. TFA is relatively weak acid ($\text{p}K_{\text{a}} \approx -0.25$), in agreement with the still lower thermal stability observed for $(\text{BImH}$ or $\text{ImH})^+(\text{TFA})^-$. As the latter two PICs are not stable in the temperature range of interest here, they were not considered for further investigation. Finally, it should be mentioned that, as shown by Kosmulski *et al.*,²⁰ dynamic TGA may considerably overrate thermal stability with respect to the case where the material is exposed to a high-temperature environment for extended time. Overall, the prepared PICs (excepting those based on TFA) exhibit good thermal stability. Such stability, however, as assessed on the basis of the above TGA results, could be in significant excess of the value exhibited under continuative exposure to high temperature. So, further work would be necessary to assess thermal stability under such operation conditions.

DSC analysis

As an example the DSC plot for $(\text{BImH})^+(\text{TFS})^-$ is shown in Fig. 4. Analogous plots (shown in Fig. S2 and S3 in the ESI†)

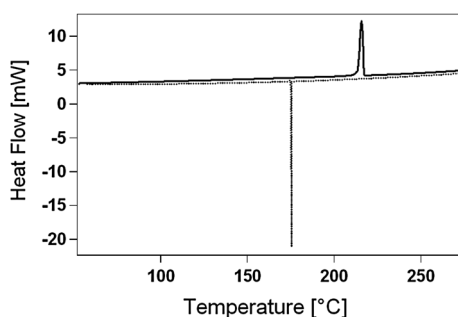


Fig. 4 DSC plot for the $(\text{BImH})^+(\text{TFS})^-$ sample. Solid line: starting heating curve. Dotted line: cooling curve.

were observed for all the other prepared PICs. The peaks at 216 and 175 °C indicate, respectively, the solid–liquid and liquid–solid transition at the chosen temperature scan-rate. Of course, the shift between the melting and crystallization temperature is understood on the basis that the sample is away from thermodynamic equilibrium during a heating/cooling cycle. Table 1 shows melting and crystallization temperatures along with related enthalpies for all the stable PICs. Actually, DSC plots of $(\text{ImH})^+(\text{TFS})^-$ and $(\text{ImH})^+(\text{NFS})^-$ exhibit one additional peak, respectively, at 34 and 62 °C upon heating. As the corresponding enthalpies are quite conspicuous (5.7 and 2.6 kJ mol^{-1} , respectively), the peak is hardly ascribable to the presence of impurities. It could more likely be ascribed to a solid–solid transition. A proper assessment of this point would require an *ad hoc* investigation, which is, however, beyond the purpose of the present work. It is worth noting in Table 1 that crystallization of the BIm-based ionic melts takes place at temperature much lower than melting point, whereas the Im-based products generally crystallize at close to melting temperature.

Ionic conductivity

Interpretation of electrochemical impedance spectra above melting point is relatively straightforward and will be presented and discussed later on. In contrast, electrochemical frequency-response of the ionic material in the crystalline state can be ambiguous. Thus, clear understanding of spectra requires more involved analysis. Fig. 5a shows the Nyquist plot for $(\text{BImH})^+(p\text{-TS})^-$ in the solid state at 150 °C. Such a plot is typical of all the other PICs prepared as far as they are in the solid state. The arc, intercepting the Z' -axis, is to be attributed to the true impedance of the sample, whereas the short tail displayed in the low-frequency region is just a spurious effect ascribable to

Table 1 Melting temperature (T_m) and enthalpy (ΔH_m), and crystallization temperature (T_c) and enthalpy (ΔH_c) for the thermally-stable PICs. Tolerance on a temperature value was typically ± 0.5 °C and in all cases less than ± 1 °C. Uncertainty on an enthalpy value is $\pm 5\%$

Sample	T_m [°C]	ΔH_m [kJ mol^{-1}]	T_c [°C]	$-\Delta H_c$ [kJ mol^{-1}]
$(\text{ImH})^+(\text{TFS})^-$	193	7.4	163	8.2
$(\text{ImH})^+(\text{NFS})^-$	176	11.1	170	9.9
$(\text{ImH})^+(p\text{-TS})^-$	147	23.4	138	22.5
$(\text{BImH})^+(\text{TFS})^-$	216	30.8	175	19.0
$(\text{BImH})^+(\text{NFS})^-$	186	29.8	139	30.5
$(\text{BImH})^+(p\text{-TS})^-$	220	27.0	134	23.7

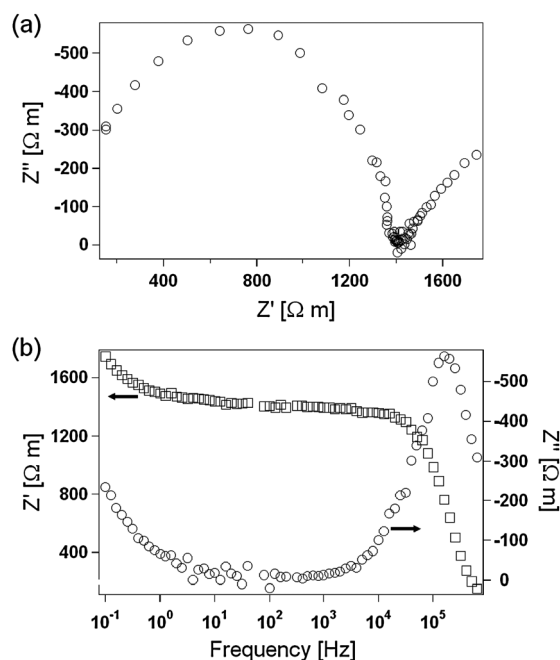


Fig. 5 (a) Nyquist and (b) Bode plots for sample $(\text{BImH})^+(p\text{-TS})^-$ in the solid state under fully anhydrous conditions at 150 °C.

impedance of electrode interface, usually modeled with a constant phase element (CPE) in the equivalent electrical circuit.²¹ Of course, analysis of data is most accurate if the frequency range is excluded where electrical response is dominated by a spurious effect due to electrode-interface impedance. In order to properly exclude such a frequency interval, it is useful to consider the frequency response of complex impedance in the Bode plot. Fig. 5b shows real (Z') and imaginary (Z'') parts of impedance as a function of frequency for $(\text{BImH})^+(p\text{-TS})^-$ in the solid state at 150 °C. Here, it is clearly observed that response from interfacial impedance is limited to a frequency range up to ≈ 10 Hz, where both Z' and Z'' vary with frequency. Above 10 Hz a plateau of Z' is encountered with the corresponding null Z'' . This region corresponds to the arc intercept with the Z' -axis in the Nyquist plot of Fig. 5a. Thus, in order to confine data analysis to response of the sole ionic material, free from spurious interfacial effects, we systematically excluded data-points at frequency below middle of the Z' -plateau in the Bode plot.

We now turn to analysis of the arc, which is the response of net bulk-sample impedance. In principle two physical models can be proposed to understand such frequency-response. One takes into account impedance of bulk crystallites as well as impedance at grain boundaries. The former is represented by a pure resistor (R_b), whereas the latter is generally modeled by a parallel of a resistor (R_{gb}) and a capacitor (C_{gb}). Of course, bulk-crystallites and grain-boundary impedances are arranged in series, resulting in the equivalent electric circuit of Fig. 6a. An alternative plausible physical model is represented in Fig. 6b. Here, grain-boundary impedance is neglected. However, bulk-crystal impedance is not modeled by a mere resistor. In fact, mechanisms of ion motion in the lattice are considered in due detail and taken into account in formulating the equivalent electric circuit. In this regard, it is useful to observe that only

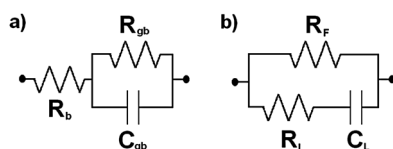


Fig. 6 Equivalent circuits for ion transport in PICs. (a) Grain-boundary model. (b) Lattice-ions/free-ions model.

“lattice” ions, not “free” ions, are present in a perfectly stoichiometric, defect-free ionic crystal. As a result, each ion can oscillate in the lattice at the local scale around the equilibrium position but cannot depart from there indefinitely, in response to an applied alternate electric field. Accordingly, no long-range ion migration is allowed. However, as defects are always present even in a stoichiometric lattice, ion migration does take place through defect sites. An additional, relevant contribution to long-range motion occurs in a non-stoichiometric lattice. Suppose, in fact, that small excess of base is present in the lattice. Then, a proton can transfer from a protonated-base site to an adjacent non-protonated-base site by a hopping-type mechanism involving covalent bonds rupture and formation. Of course, the same scenario occurs also for a stoichiometric ionic crystal in the presence of absorbed water (coming for instance from environmental humidity). In such a case absorbed water molecules explete the same function of excess base, thereby enabling long-range proton migration in the lattice according to a hopping-type mechanism. With respect to long-range ion motion, whatever the underlying mechanism, the crystal can reasonably be assumed to behave as a pure resistor from an electrical stand-point. Now, in general, both constrained ion-oscillation and long-range ion migration are allowed, especially in the presence of excess base or absorbed water. Such modes of ion motion act parallel to each other. According to this scheme, the equivalent electric circuit for the protic ionic crystal is the parallel of the complex specific-impedances related, respectively, to free ions, $Z_F(\omega)$ and lattice ions, $Z_L(\omega)$. Both terms can be determined directly from the motion equation for the involved ions in response to an applied oscillating electric field $E(\omega, t) = E_0 e^{j\omega t}$ with E_0 and ω being, respectively, field amplitude and pulsation and j imaginary unit. Denoted as x coordinate along field direction, the equation of motion for a lattice ion i with mass m_{Li} , charge q_{Li} and equilibrium position at $x_{Li} = 0$ can be written as:

$$m_{Li}\ddot{x}_{Li} = q_{Li}E_0e^{j\omega t} - k_{Li}x_{Li} - \gamma_{Li}\dot{x}_{Li} \quad (1)$$

The first term on the right-hand side is the force exerted by the electric field. The second term expresses the restoring force from the displacement to the equilibrium position. In the approximation of harmonic interaction potential, such a force is proportional to displacement x_{Li} (with elastic constant k_{Li}). This approximation is reasonable for sufficiently small displacement from equilibrium, provided it is large as compared to amplitude of thermal lattice vibration.²² Finally, from a phenomenological stand-point, the third term expresses the drag resistance due to dissipative interactions with surrounding lattice ions. This force arises as a result of the anharmonic coupling of interaction potential²³ and can generally be regarded as proportional to \dot{x}_{Li} (with apparent “viscosity” γ_{Li}).²⁴

The regime solution for eqn (1) can be found in the form $x_{Li}(\omega, t) = A_i(\omega) E(\omega, t)$ with:

$$A_i(\omega) = \frac{q_{Li}}{m_{Li}(\omega_{0i}^2 - \omega^2) + j\gamma_{Li}\omega} \quad (2)$$

where $\omega_{0i} = (k_{Li}/m_{Li})^{1/2}$ is the natural pulsation of the i th lattice ion. Accordingly, the overall current density related to lattice ions is:

$$J_L(\omega, t) = N \sum_i q_{Li} \dot{x}_{Li}(\omega, t) = j\omega N \sum_i q_{Li} A_i(\omega) E(\omega, t) \quad (3)$$

where sum is made over all ions in the elementary cell of the crystal and N is the number of elementary cells per unit volume. Then, by definition of resistivity ($J_L = \rho_L^{-1} E$), the overall complex-resistivity associated with lattice ions is expressed as:

$$\rho_L^{-1}(\omega) = j\omega N \sum_i q_{Li} A_i(\omega) \quad (4)$$

Substituting eqn (2) into eqn (4) yields:

$$\rho_L^{-1}(\omega) = \sum_i \left(r_i + \frac{1}{j\omega c_i} + j\omega \ell_i \right)^{-1} \quad (5)$$

with $r_i = \frac{\gamma_{Li}}{Nq_{Li}^2}$, $c_i = \frac{Nq_{Li}^2}{k_{Li}}$ and $\ell_i = \frac{m_{Li}}{Nq_{Li}^2}$. Each addendum in the sum is equivalent to an electrical branch made up of a resistor (of specific resistance r_i), a capacitor (of specific capacitance, or permittivity, c_i) and an inductor (of specific inductance ℓ_i) arranged in series. Thus, overall frequency response of lattice ions is equivalent to an in-parallel arrangement of these branches. The inductor impedance is only appreciable at very high frequencies (meaning $\omega \geq \gamma_{Li}/m_{Li}$). As will be shown later on, a rough estimate of γ_{Li}/m_{Li} is $\approx 10^{15}$ Hz for the investigated PICs, whereas field frequency ranges from 10^{-1} to 10^6 Hz in our EIS experiments. Therefore, the inductor contribution can safely be neglected in each branch. Moreover, it is worth noting that resistances r_i are of the same order for the various lattice ions in the elementary cell and so are capacitances c_i . As a result, the various branches must display comparable relaxation times. Accordingly, it is reasonable to expect that the parallel of these branches behaves approximately as a single series of a resistor and a capacitor of suitable resistance (R_L) and capacitance (C_L), respectively: $Z_L(\omega) = R_L + 1/j\omega C_L$ (Fig. 6b). In fact, this turns out to be so, as shown in subsequent discussion of the experimental EIS plots.

With regard to free ions, discussion proceeds with completely analogous considerations. However, no recall force is present in this case, so that $k_F = 0$. Therefore, at not too high frequencies, where an inductive effect can be relevant, free-ions impedance reduces to a real constant (a pure resistance, R_F). The corresponding resistivity is $\rho_F = \frac{\gamma_F}{n_F q_F^2}$, where n_F is the number of free ions per unit volume. In the end, the total equivalent circuit (shown in Fig. 6b) of the ionic crystalline material reduces to the parallel of R_F and $Z_L(\omega)$, with the latter being, in turn, equivalent basically to a single series of a resistor, R_L and a capacitor, C_L .

We now turn to analysis of impedance spectra utilizing comparatively both equivalent circuits of Fig. 6 as models for

the bulk-sample impedance. Both models perform semi-circles in the Nyquist plot. The experimental data-points in Fig. 5a can effectively be fitted with a circular arc; so, either model can hypothetically fit the data with suitable choice of the relevant parameters. However, careful analysis of the fitting parameters, particularly their dependence on temperature and humidity conditions, enables us to evaluate each model critically. In fact, upon employing the model of Fig. 6a, it is found that bulk-grain resistance R_b is fairly independent of temperature for all prepared PICs in the solid state. That is unrealistic, as ion transport in crystals is well known to be a strongly energy-activated process.²⁵ Moreover, the same R_b values are found for a dry and a humidified sample, whereas, as noted earlier, a dramatic decrease in R_b upon humidification must be expected for stoichiometric PICs, like the ones concerned here. Based on these observations the equivalent-circuit model of Fig. 6a must be ruled out. On the other hand, when the model of Fig. 6b is applied, exponential dependence of free-ion resistance R_F upon temperature is duly encountered. Also, a dramatic drop in R_F is registered upon sample humidification, as expected. A note concerning this model is in order here: the impedance spectrum of Fig. 5a is very nearly a circular arc, meaning that the sample does exhibit a single relaxation time. That was observed for all PICs investigated here in the solid state. Thus, our earlier approximation to lump all the branches corresponding to each lattice ion in the elementary cell into an equivalent, single branch of a resistor and a capacitor appears to be legitimated by experimental EIS observations. In summary, the equivalent-circuit model of Fig. 6b looks appropriate for a correct interpretation of impedance spectra in the solid state. Therefore, this model was utilized to determine ion-transport properties in our materials. Of course, DC conductivity is calculated based on the sole free-ions resistance R_F .

Fig. 7 shows Arrhenius plots of ionic conductivity *vs.* temperature for all prepared ionics in the solid state under fully anhydrous conditions. Experimental data-points are well fitted with an Arrhenius-type law with activation energy ranging from 0.93 to 1.33 eV, depending on the PIC (Table 2). Since we deal here with anhydrous, stoichiometric lattices, the observed long-range conduction is solely due to ion jumping through defect sites. Accordingly, the apparent energy barrier is the sum of the defect-creation energy and the ion-jumping energy.²⁶ Fitting the impedance-response arc with the model in Fig. 6b also affords determination of effective resistance R_L (resistivity r_L) and capacitance C_L (specific capacitance c_L)

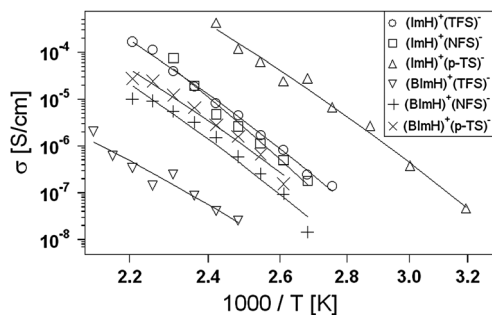


Fig. 7 Arrhenius plot for PIC conductivities in the solid state under fully anhydrous conditions. Solid lines are the linear fits.

Table 2 Activation energies (E_{att}) for PIC conductivities in the solid state under fully anhydrous conditions

Sample	E_{att} [eV]
(ImH) ⁺ (TFS) ⁻	1.15 0.03
(ImH) ⁺ (NFS) ⁻	1.33 0.10
(ImH) ⁺ (p-TS) ⁻	0.97 0.04
(BImH) ⁺ (TFS) ⁻	0.93 0.10
(BImH) ⁺ (NFS) ⁻	1.17 0.08
(BImH) ⁺ (p-TS) ⁻	1.10 0.06

associated with lattice ions. That, in turn, enables estimations of γ_{Li} ($\approx \gamma_L = r_L n_L e^2$) and k_{Li} ($\approx k_L = \frac{n_L e^2}{c_L}$), respectively, where, for uni-univalent salts like those concerned here, n_L is the number of lattice ions per unit volume and e the elementary charge. Then, a rough estimate of natural pulsations of lattice ions can also be made: $\omega_{oi} \approx (k_L/m_{Li})^{1/2}$. Values of ω_{oi} of order 10^{11} – 10^{12} Hz are found in good agreement with those calculated according to prescription of classical theory of crystalline solids.²² That further corroborates validity of the equivalent-circuit model represented in Fig. 6b for our PICs. Moreover, from determination of γ_L it is found $\gamma_L/m_{Li} \approx 10^{15}$ Hz, much larger than the maximum pulsation of the applied field (10^6 Hz), which legitimates *a posteriori* neglecting the inductance term in eqn (5). Maximum conductivity values of order 10^{-4} – 10^{-3} S cm⁻¹ are observed in the solid state for fully anhydrous conditions, with the most conducting PIC being (ImH)⁺(p-TS)⁻ ($\approx 5 \times 10^{-4}$ S cm⁻¹ at 140 °C).

Above melting temperature the arc degenerates into a single point on the Z' -axis with the Nyquist plot being simply a straight line intercepting the Z' -axis (Fig. 8). That is indicative of purely resistive behavior of the salts in the liquid state. Interpretation of impedance spectra is straightforward. In fact, plots are fitted by the series of a CPE, accounting for impedance of the melt/electrode interface and a pure resistor R_m , representing impedance of the melt. Obviously, the intercept on the Z' -axis determines just the value of resistance R_m , which in turn, affords the DC conductivity of the material. All prepared PICs generally have high melting point; so, conductivity measurements could be made over a restricted temperature range and only few data points were collected. For some of the PICs, namely those solidifying well below melting temperature, that range was extended by first heating the sample above melting point (up to 210 °C) and then cooling the melt down to solidification temperature. No conductivity data could be collected for (BImH)⁺(TFS)⁻ in the liquid state, as this salt melted at

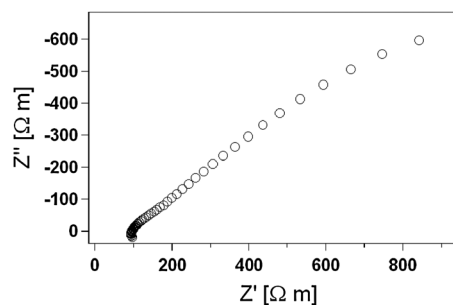


Fig. 8 Nyquist plot for sample (BImH)⁺(NFS)⁻ in the molten state under fully anhydrous conditions at 190 °C.

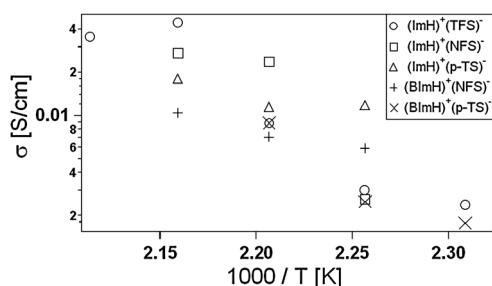


Fig. 9 Arrhenius plot for PIC conductivities in the molten state under fully anhydrous conditions.

216 °C and solidified at 175 °C. Arrhenius plots of ionic conductivity vs. temperature in the molten state are displayed in Fig. 9. Some authors reported a VTF-type relationship for amine-based PILs above melting point.¹⁰ Here, due to the restricted temperature interval with a limited number of experimental data, the points are somewhat scattered and an unambiguous analysis of conductivity- vs. temperature-behavior is not possible. However, for all PICs a sharp increase in ionic conductivity with temperature across the melting point is clearly noted, with conductivity values as high as $\approx 5 \times 10^{-2} \text{ S cm}^{-1}$ in the liquid state ((ImH)⁺(TFS)⁻ at 190 °C) under fully anhydrous conditions.

Ionic conductivity after slight humidification as described in the Experimental section was also investigated in the solid as well as molten state. It should preliminarily be noted that EIS spectra for samples in the solid state at a given temperature as recorded before melting (upon heating up) and after re-crystallization (upon cooling down) were basically identical. That suggests a likely homogeneous distribution of absorbed water throughout the sample during the whole experiment. In fact, reasonably assuming a diffusion coefficient of water in the molten sample of the order of $10^{-6} \text{ cm}^2 \text{ s}^{-1}$, a diffusion time $\tau \sim L^2/D$ no larger than a few minutes is estimated for the absorbed water to disperse over a distance $L \approx 100 \mu\text{m}$ (consistently larger than the size of the previously humidified powder granules utilized to make the pellets). Now, the samples remained in the molten state for a time interval (several hours) much greater than τ , before being cooled down and crystallized again. As a result the absorbed water certainly attained homogeneous dispersion during this lapse of time. As discussed below, EIS spectra are strongly influenced by the presence of absorbed humidity. So, the fact that spectra recorded in the solid state remained unchanged before and after melting/re-solidification, is strongly indicative that absorbed water was homogeneously dispersed even at the beginning of the whole EIS experiment. Accordingly, it is reasonable to assume that such EIS experiments were carried out under the condition of uniformly dispersed absorbed humidity. Conductivity in the solid state increases by about one order of magnitude upon exposure of the sample to ambient air for a few minutes. That has to be ascribed to predominant contribution of proton migration through non-protonated imidazole (or benzimidazole) groups in the lattice. In fact, some humidity is absorbed by the PIC during short ambient-air exposure. Absorbed water molecules act as Brønsted-base sites in the structure, causing, even in a trace

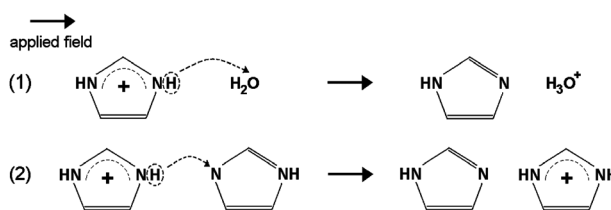


Fig. 10 Water-induced proton transport mechanism in a PIC matrix. Step (1) proton transfer from imidazole units to water molecules (acid–base reaction). Step (2) chain-transport mechanism from a protonated to an unprotonated imidazole unit.

amount, removal of a proton from (ImH)⁺ or (BImH)⁺. Then, long-range proton transport is enabled according to a chain mechanism with hopping through non-protonated Im or BIm sites as schematized in Fig. 10. Fig. 11 shows Arrhenius plots of conductivity vs. temperature for the various salts after short exposure to ambient air. Assuming Arrhenius-type behaviour in the solid state, strong scatter in the line slope was observed, corresponding to activation energies in the range of 0.23–0.92 eV. Such a notable scatter in energy values is caused by the absence of control of the humidity condition in these experiments; so, these values have to be regarded as merely indicative. However, it is clear that activation energies are significantly lower than that for the fully anhydridified PICs, unambiguously indicating that a different ion-transport mechanism sets in upon even slight humidification. Conductivity of order $10^{-3} \text{ S cm}^{-1}$ was registered for solid (ImH)⁺(NFS)⁻ at 130 °C. Also for the molten PICs ionic-conductivity values are significantly higher as compared to the case of fully-anhydrous conditions. In fact, the mechanism illustrated in Fig. 10 is not restricted to the solid state, but may take place in the liquid state as well. Also for the humidified PICs a sharp increase in conductivity is noted at the solid–liquid transition, with conductivity values of nearly $10^{-1} \text{ S cm}^{-1}$ observed in the molten state. A systematic study of conductivity as a function of humidity was not carried out as humidity could not be controlled in our experiments, except for fully-anhydrous conditions. However, it is clear that very short exposure to ambient air with presumably very small absorbed humidity produces significant enhancement of conductivity. This fact indicates strategies to develop solid or liquid ionics with potentially high proton conductivity: that is to allow for suitable excess of the Brønsted base (not necessarily water)

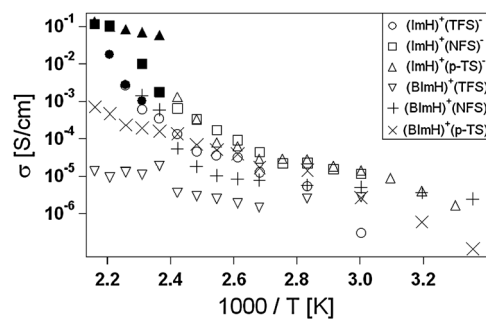


Fig. 11 Arrhenius plot for PIC conductivities after short exposure to ambient air. Empty and full symbols refer to PICs in the solid and molten state, respectively.

in the structure, thereby enabling the proton-hopping chain-mechanism depicted in Fig. 10. Of course, a closely connected problem is to stabilize (*i.e.* making non-volatile) such an excess base in the material. Effective ways to pursue this aim are currently under investigation in our laboratory.

Final remarks

In the present work protic ionic compounds have been prepared by Brønsted acid–base reaction of imidazole or benzimidazole with the one of the following acids: trifluoromethanesulfonic, nonafluorobutanesulfonic, *para*-toluenesulfonic and trifluoroacetic. All prepared compounds are thermally stable up to at least 270 °C, except for those based on trifluoroacetic acid, which were unstable above 150 °C, due to reverse reaction with contextual volatilization of the pristine acid and base. The thermally stable compounds exhibit melting temperature between 147 and 220 °C, while solidification occurs at somewhat lower temperature.

A simple physico-mathematical model for lattice-ions motion was developed and implemented to correctly interpret electrochemical impedance spectra of the compounds in the solid state, thereby enabling investigation of ionic conductivity also as a function of temperature. Arrhenius-type behavior was observed, typical of an ion-jumping mechanism through Schottky and/or Frenkel defect-sites in the lattice. Conductivity values up to $\approx 5 \times 10^{-4} \text{ S cm}^{-1}$ were measured in the solid state under fully anhydrous conditions. A sharp conductivity increase was registered across the solid–liquid transition for all compounds, with values as high as $5 \times 10^{-2} \text{ S cm}^{-1}$ in the liquid state.

A strong increase in conductivity (about one order of magnitude) is displayed by all salts in the solid state upon slight humidification by short exposure to ambient air. That is likely due to Brønsted-base behavior of absorbed water molecules, which enable proton hopping through non-protonated Im or BI_m sites by a chain-mechanism. A similar effect was observed in the molten state with conductivity values nearly approaching $10^{-1} \text{ S cm}^{-1}$.

The proton-hopping chain-mechanism enabled by absorbed water molecules inspires concepts to build effective proton transfer migration in such materials either in the solid or liquid state, by properly engineering the acid/base stoichiometry. For instance, a suitable excess of base can be pre-arranged to ensure the extensive presence of proton hopping-sites throughout the material. We acknowledge that base molecules in stoichiometric excess may be volatile and leave the material over long-term operation. We are presently developing strategies and methods to accomplish solid, protic ionic-materials with an internal network of stabilized (non-volatile) proton-hopping sites.

Acknowledgements

We thank Mr M. Basciu for his help throughout experimental work. Dr S Filippi and Dr F. Barontini of University of Pisa are gratefully acknowledged for useful help with DSC and TGA analysis, respectively. This project was financed by the Italian MIUR, PRIN 20077NCPS3_002.

References

- 1 A. J. Appleby and J. Twidell, *Philos. Trans. R. Soc. London, Ser. A*, 1996, **354**, 1681.
- 2 R. Dillon, S. Srinivasan, A. S. Aricò and V. Antonucci, *J. Power Sources*, 2004, **127**, 112.
- 3 A. S. Aricò, S. Srinivasan and V. Antonucci, *Fuel Cells*, 2001, **1**, 133.
- 4 T. Iwasita, in *Handbook of Fuel Cells – Fundamentals, Technology and Applications, Electrocatalysis*, ed. W. Vielstich, H. A. Gasteiger and A. Lamm, John Wiley & Sons, Chichester, UK, 2003, vol. 2, pp. 603–624.
- 5 Q. Li, R. He, J. Gao, J. O. Jensen and N. J. Bjerrum, *J. Electrochem. Soc.*, 2003, **150**, A1599.
- 6 R. F. Savinell, E. Yeager, D. Tryck, U. Landau, J. Wainright, D. Weng, K. Lux, M. Litt and C. Rogers, *J. Electrochem. Soc.*, 1994, **141**, L46.
- 7 J. S. Wainright, J.-T. Wang, D. Weng, R. F. Savinell and M. Litt, *J. Electrochem. Soc.*, 1995, **142**, L121.
- 8 Q. Li, R. He, J. O. Jensen and N. J. Bjerrum, *Chem. Mater.*, 2003, **15**, 4896.
- 9 K. D. Kreuer, A. Fuchs, M. Ise, M. Spaeth and J. Maier, *Electrochim. Acta*, 1998, **43**, 1281.
- 10 C. Iojoiu, P. Judenstein and J.-Y. Sanchez, *Electrochim. Acta*, 2007, **53**, 1395.
- 11 C. Iojoiu, M. Martinez, M. Hanna, Y. Molmeret, L. Cointeaux, J.-C. Lepretre, N. El Kissi, J. Guindet, P. Judenstein and J.-Y. Sanchez, *Polym. Adv. Technol.*, 2008, **19**, 1406.
- 12 H. Nakamoto and M. Watanabe, *Chem. Commun.*, 2007, 2539.
- 13 T. Yasuda, A. Ogawa, M. Kanno, K. Mori, K. Sakakibara and M. Watanabe, *Chem. Lett.*, 2009, 692.
- 14 A. Noda, Md. Abu Bin Hasan Susan, K. Kudo, S. Mitsushima, K. Hayamizu and M. Watanabe, *J. Phys. Chem. B*, 2003, **107**, 4024.
- 15 H. Nakamoto, A. Noda, K. Hayamizu, S. Hayashi, H. Hamaguchi and M. Watanabe, *J. Phys. Chem. C*, 2007, **111**, 1541.
- 16 K. Ebel and H. Koehler, *Ullmann's Encyclopedia of Industrial Chemistry*, Wiley-VCH, Weinheim D, 6th edn, 2003, vol. 17, p. 493.
- 17 H. Walba and R. Ruiz-Velasco, *J. Org. Chem.*, 1969, **34**, 3315.
- 18 H. Walba, D. L. Stiggall and S. M. Coutts, *J. Org. Chem.*, 1967, **32**, 1954.
- 19 H. Chen, T. Yan and G. A. Voth, *J. Phys. Chem. A*, 2009, **113**, 4507.
- 20 M. Kosmulski, J. Gustafsson and J. B. Rosenholm, *Thermochim. Acta*, 2004, **412**, 47.
- 21 G. Orsini and V. Tricoli, *J. Mater. Chem.*, 2010, **20**, 6299.
- 22 N. W. Ashcroft and N. D. Mermin, *Solid State Physics*, Brooks/Cole, New York, 1976, ch. 22.
- 23 N. W. Ashcroft and N. D. Mermin, *Solid State Physics*, 1976, ch. 25.
- 24 M. Born and K. Huang, *Dynamical theory of crystal lattices*, Clarendon Press, Oxford UK, 1988, ch. 7, part 46.
- 25 N. F. Mott and M. J. Littleton, *Trans. Faraday Soc.*, 1938, **34**, 485.
- 26 N. W. Ashcroft and N. D. Mermin, *Solid State Physics*, 1976, ch. 29 and 30.